2012

The Influence of Soft Spectral Components on the Structure and Stability of Warm Absorbers in Active Galactic Nuclei

Susmita Chakravorty
IUCAA, India

Ranjeev Misra
IUCAA, India

Martin Elvis
Harvard University

Ajit K. Kembhavi
IUCAA, India

Gary J. Ferland
University of Kentucky, gary@uky.edu

Monthly Notices
of the
ROYAL ASTRONOMICAL SOCIETY

Mon. Not. R. Astron. Soc. **422,** 637–651 (2012) doi:10.1111/j.1365-2966.2012.20641.x

The influence of soft spectral components on the structure and stability of warm absorbers in active galactic nuclei

Susmita Chakravorty,[1,2,3★] Ranjeev Misra,[1★] Martin Elvis,[3★] Ajit K. Kembhavi[1★] and Gary Ferland[4★]

[1]*IUCAA, Post Bag 4, Ganeshkhind, Pune 411 007, India*
[2]*Astronomy Department, Harvard University, Cambridge, MA 02138, USA*
[3]*Harvard–Smithsonian Center for Astrophysics, 60 Garden Street, Cambridge, MA 02138, USA*
[4]*Department of Physics and Astronomy, University of Kentucky, Lexington, KY 40506, USA*

Accepted 2012 January 26. Received 2012 January 26; in original form 2011 April 15

ABSTRACT

The radiation from the central regions of active galactic nuclei, including that from the accretion disc surrounding the black hole, is likely to peak in the extreme-ultraviolet ∼13–100 eV. However, due to Galactic absorption, we are limited to constrain the physical properties, i.e. the black hole mass and the accretion rate, from what observations we have below ∼10 eV or above ∼100 eV. In this paper, we predict the thermal and ionization states of warm absorbers as a function of the shape of the unobservable continuum. In particular we model an accretion disc at $kT_{\rm in} \sim 10$ eV and a *soft excess* at $kT_{\rm se} \sim 150$ eV. The warm absorber, which is the highly ionized gas along the line of sight to the continuum, shows signatures in the ∼0.3–2 keV energy range consisting of numerous absorption lines and edges of various ions, some of the prominent ones being H- and He-like oxygen, neon, magnesium and silicon. We find that the properties of the warm absorber are significantly influenced by the changes in the temperature of the accretion disc, as well as by the strength of the *soft excess*, as they affect the optical depth particularly for iron and oxygen. These trends may help develop a method of characterizing the shape of the unobservable continuum and the occurrence of warm absorbers.

Key words: galaxies: active – quasars: absorption lines – galaxies: Seyfert – X-rays: galaxies – X-rays: ISM.

1 INTRODUCTION

Accretion of matter on to a supermassive black hole and the conversion of the gravitational energy into radiation, via an accretion disc, is the main source of energy output in active galactic nuclei (AGNs). The radiation from AGNs is likely to peak in the extreme-ultraviolet (EUV) ∼10–100 eV (Lynden-Bell 1969; Pringle, Rees & Pacholczyk 1973; Shakura & Sunyaev 1973; Shields 1978; Netzer 1985). However, Galactic absorption of EUV light results in a 'blind spot' in the energy range 13–100 eV (∼912–50 Å, marked as 'unobserved' in Fig. 1) introducing an uncertainty in the shape of the spectral energy distribution (SED) of AGNs, just where it is expected to peak. Attempts have been made to reconstruct the SED from observations available below ∼10 eV and above ∼100 eV (Siemiginowska et al. 1995; Sobolewska, Siemiginowska & Zycki 2004a,b, and references therein). This unobserved part of the SED is most effective at ionizing gas (which is the very reason it also gets absorbed by the Galaxy). Hence, the continuum will influence the intervening line-of-sight gas, local to the AGN, and the resultant absorption and emission-line strengths of the various ions seen in far-UV and the Balmer continuum can be used to constrain the SED, as discussed by Netzer (1987).

At the high-energy end of the 'blind spot', that is, in the soft X-ray (0.1–10 keV), observations of most AGNs reveal that, for a majority, the SED from 2–10 keV is well approximated by a power law $f(\nu) \sim \nu^{-\alpha}$ with spectral indices ∼ 0.8. The join between the EUV (2500 Å) and the soft X-ray (2 keV), $\alpha_{\rm OX}$, is steeper, with typical values of ∼1.2 for Seyfert 1 galaxies (Netzer 1993). Hence, extending the X-ray power law to the UV cannot explain the observed flux (but see Laor et al. 1997). An ionizing continuum with two power-law components, a steep one for the join between the EUV and soft X-ray, and a flatter one for the soft X-ray SED, can represent the overall shape of the AGN spectra in the energy range 3 eV–2 keV.

However, such an SED is not a physical model and does not resemble certain specific features expected in this energy range. In particular, the proposed accretion disc, whose innermost stable orbit should have a temperature of ∼13 eV, for a black hole of mass $10^8\,{\rm M}_\odot$ and an accretion rate of $\dot{m}/\dot{m}_{\rm Edd} = 0.1$ (Shakura & Sunyaev 1973; Frank, King & Raine 2002), is not included. Another

★E-mail: schakravorty@head.cfa.harvard.edu (SC); rmisra@iucaa.ernet.in (RM); elvis@head.cfa.harvard.edu (ME); akk@iucaa.ernet.in (AKK); gary@pa.uky.edu (GF)

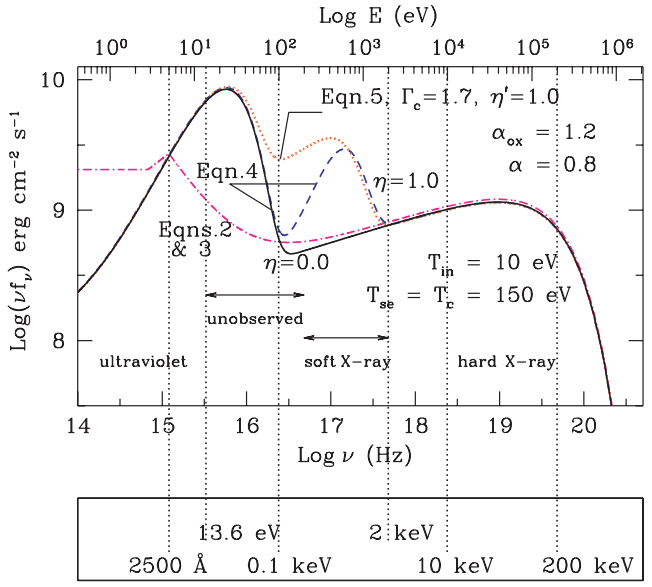

Figure 1. Comparison between various ionizing continua: the broken power law (equation 2, dot–dashed line) and more realistic SEDs having *disc-blackbody* and *soft-excess* components (equations 4 and 5). For all the curves, $\alpha = 0.8$ and $\alpha_{\rm OX} = 1.2$. Using equation (4) we draw the solid curve with $\eta = 0.0$ and the dashed curve with $\eta = 1.0$, while the dotted curve is drawn using equation (5) with $\eta' = 1.0$. The temperature of the innermost ring of the accretion disc is $T_{\rm in} = 10$ eV and the temperature corresponding to the *soft excess* is $T_{\rm se} = T_{\rm c} = 150$ eV. See text for further details.

spectral component which would remain unaccounted for by a simple two-power-law continuum is the *soft excess* which is seen in most AGNs below 2 keV. The *soft excess* could be a Comptonized disc component (Czerny & Elvis 1987), an additional quasi-blackbody (Ross & Fabian 1993, 2005; Korista, Ferland & Baldwin 1997; Crummy et al. 2006) or due to relativistic broadened absorption features (Gierlinski & Done 2004). Such spectral components are likely to have important effects on the nature of the absorbing gas along the line of sight towards the central engine of the AGN.

In the 0.3–1.5 keV soft X-ray spectra of about half of all Seyfert 1 galaxies (Nandra & Pounds 1994; Reynolds 1997; George et al. 1998) and quasars (Piconcelli et al. 2005), one can find signatures of photoionized gas called 'warm absorbers' (WAs, Halpern 1984). These signatures are, often, absorption lines and edges from highly ionized species, such as O VII, O VIII, Fe XVII, Ne X, C V and C VI (Collinge et al. 2001; Kaastra et al. 2002; Kinkhabwala et al. 2002; Blustin et al. 2003; Krongold et al. 2003; Netzer et al. 2003; Turner et al. 2004). The typical column density observed for the gas is $N_{\rm H} \sim 10^{22\pm1}$ cm^{-2}. The ionization parameter ξ of the WA spans a range $\sim$10–1000 erg cm s^{-1} corresponding to gas temperatures of 10^4–$10^{6.5}$ K. Some authors claim that the WA is made up of discrete thermodynamic phases in near pressure equilibrium (Andrade-Velazquez et al. 2010, and references therein), while others (Ogle et al. 2004; Steenbrugge et al. 2005; Behar 2009) believe that the gas has a continuous distribution of temperature and pressure.

In this temperature range, heating and cooling processes are, respectively, dominated by photoionization and recombination of higher ionization states of heavier elements. These processes result in local regions of thermal stability in this otherwise unstable temperature range (Krolik, McKee & Tarter 1981; Gehrels & Williams 1993; Hess, Kahn & Paerels 1997). Chakravorty et al. (2009) showed that the nature of the WA is strongly influenced by the chemical composition of the absorbing gas. It was shown that the abundance of iron and oxygen, which have important atomic transitions in the sub- keV energy range, is particularly important.

To obtain the equilibrium conditions for a gas with an assumed set of physical conditions, we have used the publicly available photoionization code CLOUDY[1] version C07.02 (see Ferland et al. 1998). CLOUDY calculates the ionization equilibrium conditions by solving the energy and charge conservation equations under the assumption that all the atomic processes have had time to reach a steady state. Any stable photoionized gas will lie on the thermal equilibrium curve (hereafter referred to as the *stability curve*) where heating balances cooling. The stability curve of temperature (T) against pressure (ξ/T), where ξ is the ionization parameter (see below for definition), is often used to study the nature of the WA. Gas lying off the stability curve will heat or cool until reaching the curve. If the curve has kinks that produce multiple stable values at fixed ξ/T, then the WA can have multiple temperature phases in pressure equilibrium. The shape of the stability curve depends on the SED of the ionizing continuum and the chemical abundance of the gas (Reynolds & Fabian 1995; Komossa & Meerschweinchen 2000; Komossa & Mathur 2001; Krolik & Kriss 2001; Chakravorty et al. 2008, 2009).

In this paper, we investigate the behaviour of the stability curve as a function of *disc blackbody* and *soft excess* both to understand the role of these spectral components in the nature of the WA and to examine whether the observable parameters of the WA can diagnose the shape of the AGN continuum in the EUV 'blind spot'. In Section 2, we describe the different models of the AGN continuum that we are interested in and use these SEDs to study their effect on the stability curves in Section 3. We investigate the causes of the variations in the stability curves in Section 4 by studying the heating and ionization fractions of the elements and ions which are responsible for determining the nature of the WA. Section 5 examines the relevance of a few other physical parameters, like the X-ray slope of the ionizing continuum and the abundance of the absorbing gas (also discussed in Chakravorty et al. 2009) in the context of this study. The multiphase nature of the WA is discussed in Section 6 and we conclude our results in Section 7.

2 THE AGN CONTINUUM

The 2–10 keV X-ray spectra of most of the observed AGNs can be modelled satisfactorily using a power law $f(\nu) \sim \nu^{-\alpha}$ where the spectral index α for most AGNs lies in the range $0.7 < \alpha < 0.9$ (Wilkes & Elvis 1987; Grupe et al. 2006; Lopez et al. 2006). The optical depth $\tau = 1$ for photons at 0.2 keV with a typical Galactic hydrogen column density of $N_{\rm H} = 3 \times 10^{20}$ cm^{-2}. Extinction is a steeply rising function of column density, for example, $\tau = 2$ at 0.2 keV for $N_{\rm H} = 5 \times 10^{20}$ cm^{-2}. Thus, we lack observational constraints on the evolution of the X-ray power law at lower energies. However, for most AGNs, the UV flux is found to be much higher than what a simple extrapolation of the X-ray power law to lower energies would predict (Elvis et al. 1994; Zheng et al. 1997; Shang et al. 2005), but see Laor et al. (1997) for exceptions. The slope $\alpha_{\rm OX}$, defined as

$$\alpha_{\rm OX} = -0.384 \log \left[\frac{f(2\,{\rm keV})}{f(4.7\,{\rm eV} = 2500\,{\rm \AA})} \right] \quad (1)$$

by Tananbaum et al. (1979), is conventionally used to parametrize the nominal power law between the UV and soft X-ray bands. The

[1] URL: http://www.nublado.org/

observed range is $1 \lesssim \alpha_{\rm OX} \lesssim 2$ (Stalin et al. 2009; Green et al. 2009, and references therein).

The overall shape of the AGN continuum in the energy range of ∼4.7 eV (2500 Å) to 10 keV can thus be represented as a sum of two power-law components:

$$f(\nu) \sim \left(\nu^{-\alpha} + A_1 \nu^{-\alpha_{\rm s}}\right) {\rm e}^{-\frac{\nu}{\nu_{\rm max}}}, \quad \text{for } E(=h\nu) \geq 4.7\,{\rm eV}, \qquad (2)$$

where $\alpha_{\rm s}(>0)$ is the spectral index of a steep soft component and A_1 is the relative normalization factor to realize the desired values of $\alpha_{\rm OX}$ (dot–dashed curve in Fig. 1). Chakravorty et al. (2009) had used such an SED with $E_{\rm max} = h\nu_{\rm max} = 200$ keV, and this value is maintained throughout this paper, as well. Results from the *Swift*/Burst Alert Telescope hard X-ray sky survey (Tueller et al. 2008) show that, of the brightest few dozen AGNs, for which $E_{\rm max}$ can be determined, the cut-off spans the range 50–450 keV. In Chakravorty et al. (2009) we have shown that in the range $50 < E_{\rm max} < 400$ keV, the variation in $E_{\rm max}$ does not have any significant effect on the nature of the WA. For energies lower than 4.7 eV, Chakravorty et al. (2009) followed the cut-off scheme

$$\begin{aligned} f(\nu) &\sim \nu^{-0.5} \quad \text{for } 2.8 \leq E(=h\nu) < 4.7\,{\rm eV}, \\ &\sim \nu^{-1.0} \quad \text{for } 0.12 \leq E(=h\nu) < 2.8\,{\rm eV}, \\ &\sim \nu^{2.5} \quad \text{for } E(=h\nu) < 0.12\,{\rm eV}. \end{aligned} \qquad (3)$$

This scheme is similar to that described by Mathews & Ferland (1987). However, a SED described by equations (2) and (3) may sometimes be an inadequate description for the AGN ionizing continuum because it fails to represent the signature of the accretion disc at ∼10 eV or the *soft-excess* component.

2.1 Disc blackbody

Multiwavelength observations suggest that the AGN continua peak in the EUV energy band and emission here usually dominates the quasar luminosity (Shields 1978; Neugebauer et al. 1979; Malkan & Sargent 1982; Elvis et al. 1986; Czerny & Elvis 1987; Mathews & Ferland 1987; Laor 1990; Siemiginowska et al. 1995; Zheng et al. 1997; Sobolewska et al. 2004a,b). This spectral component, often referred to as the 'Big Blue Bump', is considered to be the signature of the presence of an accretion disc as discussed by Lynden-Bell (1969), Pringle et al. (1973), Shields (1978) and Shakura & Sunyaev (1973).

According to the standard theory of accretion discs by Shakura & Sunyaev (1973), the emission from the disc can be modelled as a sum of local blackbody radiations emitted from annuli of the disc at different radii. The temperature of all the subsequent rings can be estimated from the theory if the temperature $T_{\rm in}$ of the innermost ring of the accretion disc is known, which in turn is related to the one-fourth power of the mass of the central black hole and to the fourth power of its accretion rate. Thus, for the same accretion rate, $T_{\rm in}$ changes by only a factor of 3 while the black hole mass spans a range of about two orders of magnitude. As such, the resultant shape of the 'Big Blue Bump' peaks between ∼10 and 100 eV for the range of black hole masses and accretion rates typical of Seyfert galaxies.

Studies of high-redshift quasars show that their UV–EUV SEDs are consistent with the standard theory of accretion discs (Bechtold et al. 1994; Page et al. 2004a,b; Shang et al. 2005). However, typically, the quasars have higher mass ($10^8 \lesssim M_{\rm BH} \lesssim 5 \times 10^{10}\,{\rm M}_\odot$; Bechtold et al. 1994; Shang et al. 2005) and higher accretion rates (Bechtold et al. 1994). Thus, for the same accretion rates, we can expect the 'Big Blue Bump' in quasars to be peaking at lower energies than that in Seyferts which would typically result in steeper $\alpha_{\rm OX} \sim 1.8$ (Bechtold et al. 1994) for the quasars, as compared to 1.2 (Netzer 1993) for the Seyferts.

A standard model for the spectral component from the accretion disc is available as *disc blackbody* (Mitsuda et al. 1984; Makishima et al. 1987) in XSPEC[2] (Arnaud 1996). We have used version 11.3 of XSPEC to generate the *disc-blackbody* spectral component $f_{\rm dbb}(\nu)$ to be used in the construction of the realistic AGN continuum (the third term in equations 4 and 5). The solid black line in Fig. 1 shows a SED which includes a 'Big Blue Bump' with $T_{\rm in} = 10$ eV. In this paper, we explore 'Big Blue Bumps' in the range $10 \leq T_{\rm in} \leq 30$ eV corresponding to $10^{8.47} \leq M_{\rm BH} \leq 10^{6.56}\,{\rm M}_\odot$ for an accretion rate of $\dot{m}/\dot{m}_{\rm Edd} = 0.1$. This range of accretion disc parameters pertain to Seyfert galaxies or low-mass and low accretion rate quasars. We do not explore the parameter range for higher mass quasars because for them $T_{\rm in}$ would move to lower energies and such *disc blackbodies* are less likely to influence the nature of the WA.

2.2 Soft excess

X-ray observations of AGNs with *ROSAT* and *XMM–Newton* often show that if the 1–10 keV power law is extended to lower energies to fit the observed spectra of type 1 AGNs, some unaccounted for excess intensity is usually seen at $E < 1$ keV (Elvis, Wilkes & Tananbaum 1985; Brinkmann 1992; Buehler et al. 1995; Pounds & Reeves 2002). This excess has come to be known as the *soft-excess* component. A blackbody with temperature $T_{\rm se} \sim$ 100–200 eV (i.e. peaking at ∼282–564 eV) is often a good fit to the *soft excess* (Matsumoto, Leighly & Marshall 2004; Porquet et al. 2004; Piconcelli et al. 2005; Vignali et al. 2004, and references therein). The same authors show that the ratio of the *soft-excess* luminosity to power-law luminosity, usually between 0.1 and 10 keV, varies from object to object from 0.04 in Mrk 304 (Piconcelli et al. 2005) to $\gtrsim$1.0 in Ark 564 (Vignali et al. 2004). The simple 'sum of blackbodies' model for the accretions disc is a satisfactory qualitative representation of the UV SED with a range of parameter values to cover the observed AGN properties. However, all AGN discs, having supermassive black holes at their centres, are too cold to reach soft X-rays at ∼0.5 keV. More sophisticated modifications of this model (Czerny & Elvis 1987; Korista et al. 1997) or an additional spectral component is required to explain the *soft excess*.

2.2.1 *Blackbody soft excess*

A theoretical representation of the *soft excess* as a blackbody is a simplified version of the Ross & Fabian (1993, 2005) model for the *soft-excess* component which owes its origin to the reflection of the power-law component of the AGN spectrum from the accretion disc. Thus, in this model the X-ray power-law photons are reprocessed, instead of the ones from the accretion disc.

The general SED for the ionizing continuum including a blackbody *soft-excess component* can be given as

$$f(\nu) \sim \left[\left\{ \nu^{-\alpha} + \eta \frac{2\pi h}{c^2} \frac{\nu^3}{\exp(h\nu/k_{\rm B}T_{\rm se}) - 1} \right\} + A_2 f_{\rm dbb}(\nu, T_{\rm in}) \right] {\rm e}^{-\frac{\nu}{\nu_{\rm max}}}. \qquad (4)$$

[2] http://heasarc.gsfc.nasa.gov/docs/xanadu/xspec/

The first term in the above equation represents the X-ray power law with spectral index α. The second term is the *soft-excess* component, as a blackbody distribution of photons, where $T_{\rm se} = 150\,{\rm eV}$ is the temperature of the blackbody and η determines the ratio of luminosity in the *soft-excess* component to that in the power law between 0.1 and 10 keV. The third term in equation (4) is the *disc-blackbody* component which is parametrized by $T_{\rm in}$, the temperature of the innermost ring of the accretion disc. A_2 is the normalization factor to attain the desired value of $\alpha_{\rm OX}$. Unless otherwise mentioned, throughout this paper, we have used $\alpha = 0.8$ and $\alpha_{\rm OX} = 1.2$, $E_{\rm max} = h\nu_{\rm max} = 200\,{\rm keV}$. For numerical convenience, we put a cut-off for $f(\nu)$ at $E = h\nu = 0.12\,{\rm eV}$ below which the flux drops off as $\nu^{2.5}$.

In Fig. 1 both the black solid SED and the blue dashed SED are drawn using equation (4). For both SEDs, $T_{\rm in} = 10\,{\rm eV}$ so that the peak of the disc blackbody lies at ∼30 eV. The solid line represents a SED which does not have any *soft-excess* component, that is, $\eta = 0$. On the other hand, the blue dashed SED with $\eta = 1.0$ has a moderately strong *soft excess*. See further discussions in Section 3.3.1.

2.2.2 *Comptonization by ∼150 eV plasma*

Korista et al. (1997) discuss the puzzle that many quasars which show soft ionizing continuum would have an insufficient number of photons at the 54.4 eV He II edge to generate the observed strength of He II emission seen in the same objects. To explain the strength of the He II line in Mrk 335, Korista et al. (1997) invoked a 'double-peaked' UV–EUV continuum where the second 'bump' peaks at ∼54 eV and contains energy comparable to the classical UV bump at lower energies (∼10 eV).

A model, where the photons from the accretion disc are upscattered by inverse Comptonization due to energetic electrons, does a better job of qualitatively satisfying the required strength of the UV–EUV SED for objects like Mrk 335. Czerny & Elvis (1987) have shown that the models which account for the electron scattering of the accretion disc photons are better than the simple 'sum of blackbodies' model. Similar thermal Comptonization models have been worked out by Lightman & Zdziarski (1987), Coppi (1992), Haardt & Maraschi (1993), Coppi (1999) and Beloborodov (1999) among others.

The thermal Comptonization model of Lightman & Zdziarski (1987) has been used by Zdziarski, Johnson & Magdziarz (1996) and extended by Zycki, Done & Smith (1999) and their model is included in XSPEC 12.5 (Arnaud 1996) as *nthcomp*. We have used *nthcomp*, where we have assumed that the seed photons coming from the accretion disc (modelled as *disc blackbody*) are reprocessed by the thermal plasma to generate sufficient photons at sub-keV to mimic the *soft excess*, usually observed in AGNs. The high energy cut-off for the resulting *soft-excess* feature is parametrized by the electron temperature $T_{\rm c}$, whereas the low-energy rollover is dependent on the effective temperature of the seed photons from the accretion disc, which in this case is parametrized by $T_{\rm in}$. Between the low- and high-energy rollovers, the shape of the spectrum is not necessarily a power law, but can be parametrized by an asymptotic power-law index $\Gamma_{\rm c}$ which would physically be determined by the combination of electron scattering optical depth and electron temperature, that is, by the Compton-y parameter (Rybicki & Lightman 1986). Beloborodov (1999) had shown that there is a simple relation $\Gamma_{\rm c} \approx \frac{9}{4} y^{-2/9}$ between the power-law index and the Compton-y parameter. Thus, in our model, $\Gamma_{\rm c}$, used as an input, gives a measure of the extent of Compton reprocessing; that is, the larger the value of $\Gamma_{\rm c}$, the lesser is the number of photons reprocessed from the *disc-blackbody* component to the high-energy photons at $\sim T_{\rm c}$.

The SED with this alternative model for the *soft excess* $f_{\rm c}(\nu)$, generated by *nthcomp*, can be written as

$$f(\nu) \sim [\,\{\nu^{-\alpha} + \eta' f_{\rm c}(\nu, T_{\rm in}, T_{\rm c}, \Gamma_{\rm c})\} + A_2 f_{\rm dbb}(\nu, T_{\rm in})\,]\, {\rm e}^{-\frac{\nu}{\nu_{\rm max}}}, \quad (5)$$

where η' is the ratio of luminosity of the *soft-excess* component for $E(= h\nu) \geq 0.3\,{\rm keV}$ to the luminosity of the power-law component in the energy range 0.1–10 keV. The orange dotted curve in Fig. 1 is drawn using 5 with $T_{\rm in} = 10\,{\rm eV}$, $T_{\rm c} = 150\,{\rm eV}$, $\eta' = 1.0$ and $\Gamma_{\rm c} = 1.7$. Note that at $E = 54.4\,{\rm eV}$ (i.e. $\log \nu = 16.12$) the orange dotted SED has 1.4 times higher flux than the blue dashed SED due to a blackbody *soft excess* and this factor grows to 13.1 at $E = 100\,{\rm eV}$. Thus, SEDs like the orange dotted line are better suited to explain observations of objects like Mrk 335 or Mrk 478. See further discussions on this issue in Section 3.3.2.

Chakravorty et al. (2009) showed that the WA temperature range, $10^{4.5} < T < 10^{6.5}\,{\rm K}$, is strongly influenced by the chemical composition of the absorbing gas, particularly by the abundance of iron and oxygen which have important atomic transitions in the sub-keV energy range where the *soft-excess* component is likely to have maximum effect. In the following sections, we shall extensively investigate the effect of SEDs, given by equations (4) and (5), on the nature of the WA, as a function of the shape of the accretion disc component parametrized by the value of $T_{\rm in}$, and the strength of the *soft-excess* feature parametrized by η or $\Gamma_{\rm c}$ and η'.

3 STABILITY CURVE ANALYSIS

Studies of WA variability in response to continuum changes show that it is reasonable to assume the WA to be in ionization and thermal equilibrium as observed for NGC 985 (Krongold et al. 2005a), NGC 3783 (Krongold et al. 2005b) and NGC 5548 (Andrade-Velazquez et al. 2010). The thermal and ionization equilibria are governed by heating due to photoionization and cooling due to line emission and collisional recombination (radiative and dielectronic).

We model the WA as an optically-thin, plane-parallel slab of solar metallicity gas [as given by Allende Prieto, Lambert & Asplund (2001, 2002) for C and O, by Holweger (2001) for N, Ne, Mg and Si, and by Grevesse & Sauval (1998) for the remainder of the first 30 elements] with column density $N_{\rm H} = 10^{22}\,{\rm cm}^{-2}$. The absorbing gas is assumed to be illuminated by an ionizing continuum given by equation (4) or (5) and the ionization state of the gas can be described by specifying the ratio of the ionizing photon flux to the gas density through an *ionization parameter* (see equation 6).

3.1 Normalizing the ionization parameter

The photoionization state of the WA can be parametrized by the ionization parameter which is the ratio of the ionizing photon flux to the gas density (Tarter, Tucker & Salpeter 1969):

$$\xi = L_{\rm ion}/n_{\rm H} R^2 = \int_{h\nu_0 = 13.6\,{\rm eV}}^{13.6\,{\rm keV}} \frac{L_\nu}{n_{\rm H} R^2}\, {\rm d}\nu \qquad ({\rm erg\,cm\,s^{-1}}), \quad (6)$$

where $L_{\rm ion}$ is the luminosity between 13.6 eV and 13.6 keV (i.e 1–10^3 Rydberg). Hence, $\xi/T \sim L/pR^2$, p being the gas pressure in the WA.

This definition has a certain drawback which is demonstrated by the stability curves in the left-hand panel of Fig. 2. The dot–dashed curve is for a gas illuminated with the broken power-law

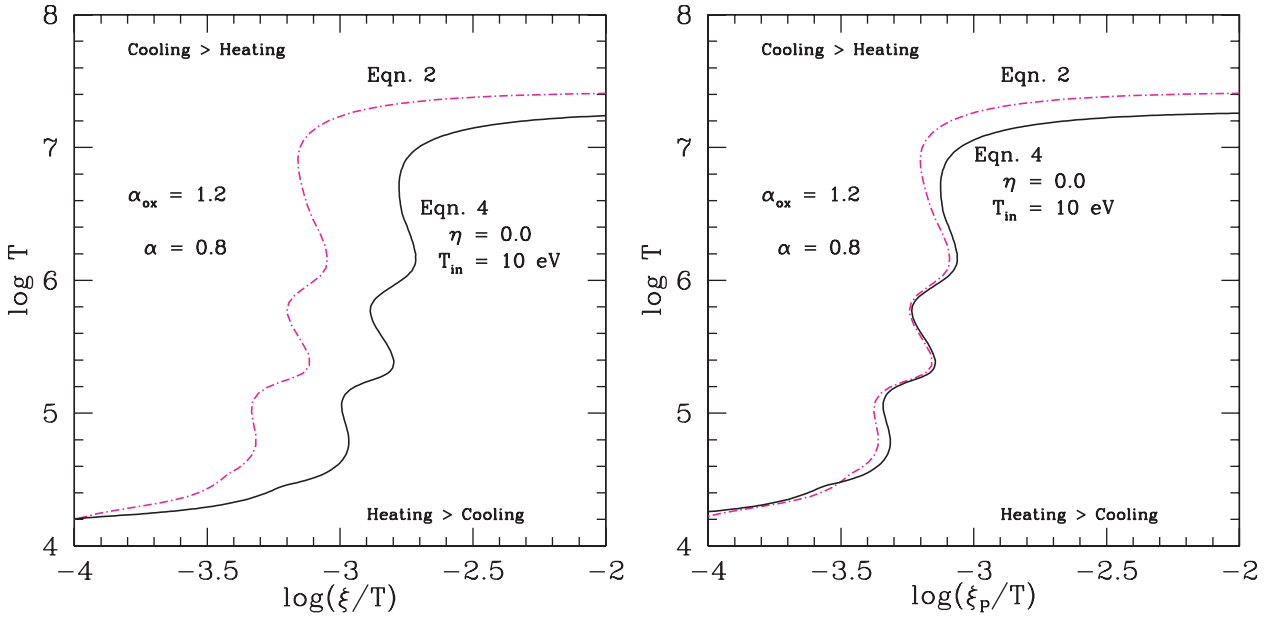

Figure 2. Stability curves demonstrating the advantage of using ξ_P compared to ξ. The dot–dashed stability curves in both the panels are drawn using the broken-power-law continuum (equation 2), whereas the solid ones are generated for a SED given by equation (4) with $\eta = 0.0$ and $T_{in} = 10$ eV. The curves drawn with ξ (left-hand panel) are separated in the phase space even if the WA in both the cases has similar nature. On the other hand, the curves drawn using the alternative definition, ξ_P, of the ionization parameter (right-hand panel) are almost identical showing the true nature of the WAs. See Section 3.1 for further details.

ionizing continuum (equation 2) and the solid curve is generated with a more realistic SED given by equation (4), having an accretion disc component with $T_{in} = 10$ eV, but no *soft excess* ($\eta = 0.0$). From Fig. 1 we can see that the SED including the accretion disc component (solid black line) has ∼50 times more photons at 13.6 eV (1 Rydberg) than the dot–dashed spectra (equation 2), although they have similar flux at 100 eV. This would result in very different values of ξ in the two cases but very similar WAs, since the WA properties are determined by the photon distribution in the soft X-ray ($E \gtrsim 100$ eV) and not by photons with energy $E \ll 100$ eV. The *kinks* in any stability curve are a result of the interplay between the various heating and cooling agents responsible for maintaining the gas at a state of thermal equilibrium (Chakravorty et al. 2008, 2009). The stability curves in the left-hand panel of Fig. 2 have almost identical shape for $4.4 < \log T < 6.5$, indicating that they have WAs with identical thermal properties and state of ionization. However, they are separated from each other, by a mere horizontal shift in $\log(\xi/T)$ because of the different ξ values predicted by the two different SEDs. Thus, ξ is a relatively poor parametrization of the nature of the WA. Such a problem with the standard definition of the ionization parameter has been acknowledged by other authors as well. For example, Chelouche & Netzer (2005, and references therein) use an ionization parameter U_x which considers the ionizing flux only between 540 eV and 10 keV.

To circumvent this problem, we use a normalization scheme, appropriate for this paper, as described in the following. All the SEDs considered in this paper (except for ones in Section 5.1) have a common power law in addition to the disc-blackbody and/or the *soft-excess* component. Hence, we define

$$\xi_P = \frac{L_P}{n_H R^2} = \frac{1}{n_H R^2}\left(4\pi R^2 \int_{h\nu_0=13.6\ \mathrm{eV}}^{200\ \mathrm{keV}} \nu^{-\alpha}\, \mathrm{d}\nu\right), \qquad (7)$$

where L_P is a constant luminosity due to the soft X-ray power-law component $f(\nu) \sim \nu^{-\alpha}$ (with $\alpha = 0.8$) in the energy range $E = h\nu =$ 13.6 eV–200 keV. Thus, ξ_P is the ratio of the ionizing flux, due only to the power-law component in the energy range 13.6 eV–200 keV, to the gas density. For any SED given by equation (2), (4) or (5), there would be a unique factor ξ/ξ_P for the same $n_H R^2$. The stability curves corresponding to the ionizing continua given by equation (2), (4) or (5) are calculated by CLOUDY taking the entire SEDs into account, following which their x-axis [$\log(\xi/T)$] is divided by the unique (to each SED) factor ξ/ξ_P generating a normalized stability curve in the $\log T$–$\log(\xi_P/T)$ plane. The advantage of such a normalization is shown in the right-hand panel of Fig. 2, where the stability curves overlap closely, demonstrating the true physical scenario of two very similar WAs. Note that these are the same stability curves which are separated by the horizontal shift in the left-hand panel, as discussed above. This normalization scheme is used for all subsequent figures in this paper except for Fig. 9 (shown later). In addition to the SEDs which determine the physics of the respective stability curves, the top panels of Figs 3, 4 and 5 also include the constant power-law component (magenta long-dashed–short-dashed curve) which is used to normalize the stability curves so that they can be plotted in terms of $\log(\xi_P/T)$.

It is to be noted that while calculating the thermal and ionization properties of the WA, CLOUDY uses the entire SEDs, including all three spectral components (namely the *disc blackbody*, the *soft excess* and the X-ray power law), described by equations (4) and (5). The introduction of ξ_P and normalization of the stability curves is only for the convenience of demonstration of the stability curves and their associated properties. Use of ξ_P merely introduces an overall horizontal shift in these distributions. Further, note that any given range in $\log(\xi/T)$ would correspond to an exactly equal range in $\log(\xi_P/T)$ and vice versa.

3.2 Disc blackbody

The top panel of Fig. 3 shows the ionizing continua which include the *disc-blackbody* and the power-law components ($\eta = 0$,

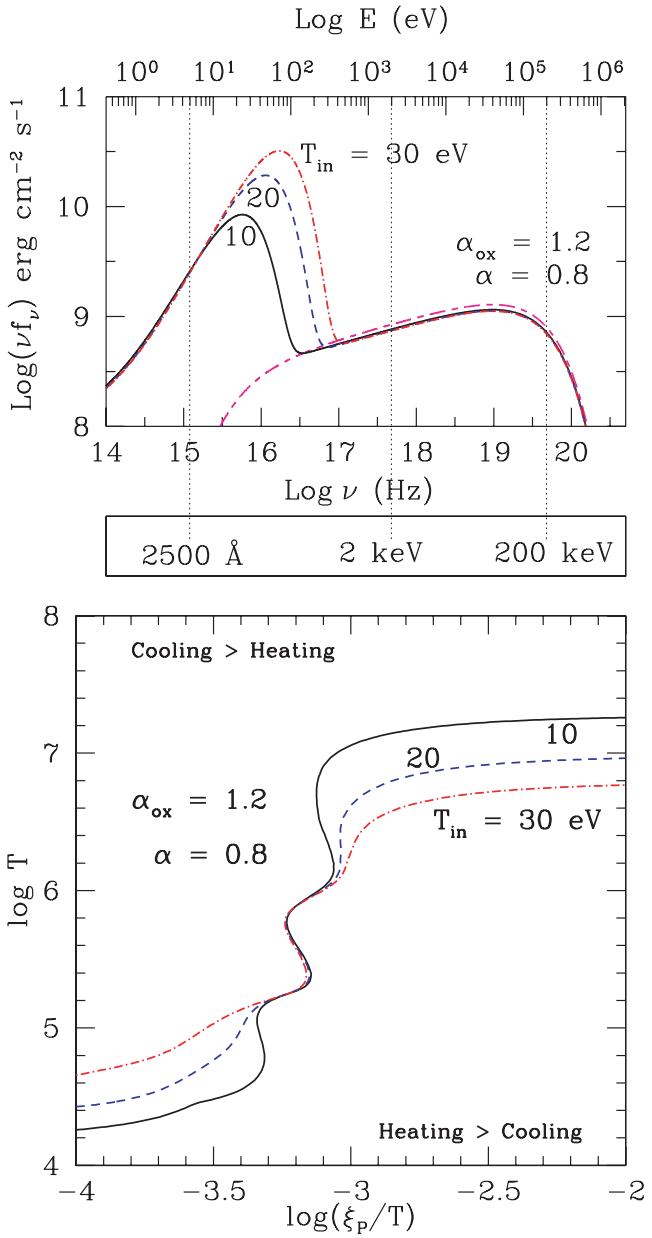

Figure 3. The SEDs in the top panel are constituted by two spectral components, an X-ray power law and an EUV *disc blackbody*. The curves are for different values of the temperature, $T_{\rm in}$, of the innermost ring of the accretion disc. $\alpha = 0.8$ and $\alpha_{\rm OX} = 1.2$ for all the SEDs. We have included the constant power law (magenta long-dashed–short-dashed curve) which is used to normalize the stability curves so that they can be plotted in terms of $\log(\xi_{\rm P}/T)$. Important energy values including the upper energy cut-off ($E_{\rm max} = 200$ keV) and the range of definition for $\alpha_{\rm OX}$ (2500 Å and 2 keV) have been marked and labelled. The bottom panel shows the stability curves corresponding to the ionizing continua shown in the top panels.

equation 4). As $T_{\rm in}$ is increased from 10 to 30 eV, the peak of the flux distribution moves from ∼30 to 90 eV. Photons at $E \lesssim 90$ eV affect only the lower ionization species of the absorbing gas. The resulting WA should show differences only in the nature of the lower ionization phases, and should have very similar higher ionization states. We shall discuss this issue further in Section 4.

Corresponding stability curves are shown in the bottom panel of Fig. 3. A hotter *disc blackbody* lowers the Compton temperature branch and increases the temperature of the bottom branch. However, in the $5 < \log T < 6.5$ K temperature range of, the WAs, the stability curves are independent of the value of $T_{\rm in}$, that is, unaffected by the spectral component due to the accretion disc. However, the lower temperature ($\log T < 5$) part of the stability curves undergoes remarkable change with the increase in $T_{\rm in}$; for the same value of $\xi_{\rm P}$, the gas attains a higher temperature, the stability curve becomes more stable and any possibility of multiphase existence with higher ionization states is lost. See Section 6 for further discussion on this issue.

3.3 Soft excess

3.3.1 Blackbody soft excess

The top panel of Fig. 4 shows the ionizing continua given by equation (4) with the values of $\eta = 0.0$, 1.0 and 3.0, representing increasing strengths of the *soft-excess* component for a fixed value of the blackbody temperature $T_{\rm se} = 150$ eV. The corresponding stability curves in the bottom panel show a remarkable enhancement of the stable $\log(\xi_{\rm P}/T)$ range from ∼0.20 through 0.41 to 0.63 dex for the 10^5-K absorber, as the strength of the *soft excess* is increased from $\eta = 0.0$ through 1.0 to 3.0. The 10^6-K phase remains unchanged through the variation in η. In the $\eta = 3.0$ case, however, the transition from the $\sim 10^5$ to 10^6 K phase is smooth, that is, with no distinct unstable region separating the two temperature regimes. Such a result implies that the stronger the *soft-excess* component in the spectra, the greater is the probability of finding an $\sim 10^5$ K absorber, since the stable region then becomes less susceptible to luminosity variations in the AGN. However, the possibility of the 10^5 K gas being in pressure equilibrium with the other WA phases is significantly reduced. We shall return to these points in Section 6.

To find a typical value of η implied by X-ray observations of AGNs, we refer to two examples, namely a typical Seyfert 1 galaxy NGC 5548 and a narrow-line Seyfert 1 galaxy IRAS 13349+2438. Andrade-Velazquez et al. (2010) analysed the 800-ks *Chandra* grating spectra of NGC 5548 and their best-fitting parameters for the soft X-ray continuum is a power law with $\alpha = 0.6$ and a blackbody with $T_{\rm se} = 110$ eV. The relative normalization of the two components results in $\eta \sim 1.2$. Similarly, Holczer, Behar & Kaspi (2007) have analysed the 300-ks *Chandra* data for IRAS 13349+2438 and have reported the spectral parameters for the best-fitting ionizing continuum comprising of a X-ray power law with $\alpha = 0.9$ and a blackbody with $T_{\rm se} = 105$ eV. From their results we calculate η to be ∼2.58. In both cases, the values of η are well within the range considered here (0–3).

The $T_{\rm se}$, observed for a large number of type I AGNs, lies in the small range 100–200 eV. We have checked whether the influence of the *soft-excess* component is modified when the blackbody temperature is varied across this range. Results showed that the stability curves remain unaffected by such variations, for example, the range in $\log(\xi_{\rm P}/T)$ for the stable 10^5-K gas changes by merely 0.06 dex as $T_{\rm se}$ varies from 100 to 200 eV.

3.3.2 Comptonized soft excess

The blackbody *soft excess* sometimes turns out to be inadequate in explaining the observations. For example, the SED for Mrk 478 may be one to three times brighter in νL_ν at $E \sim 120$ eV than it is at 1300 Å (∼10 eV) (Gondhalekar et al. 1994; Marshall et al. 1996). We find that a blackbody *soft excess* cannot satisfy such a condition even with a relatively high normalization of $\eta = 3.0$ (top

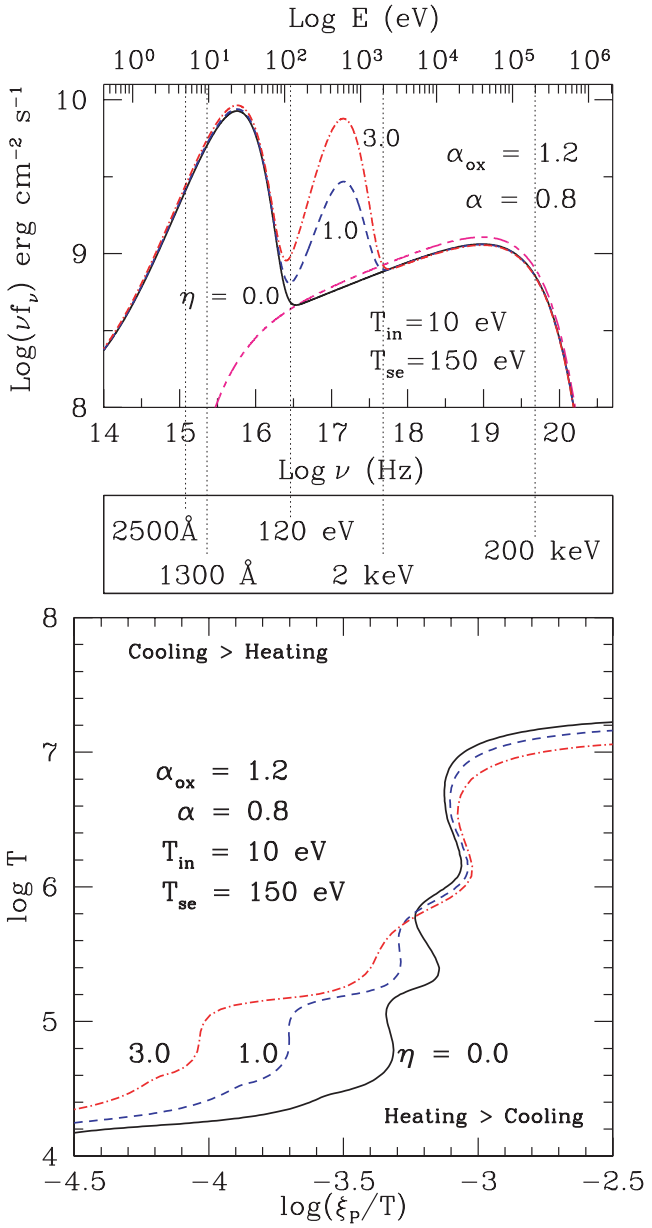

Figure 4. Top panel: SEDs which have a *soft-excess* component described by a blackbody distribution (see equation 4) with temperature $T_{se} = 150$ eV. The different SEDs are for different values of η, that is, for different strengths of the *soft-excess* component. $\alpha = 0.8$ and $\alpha_{OX} = 1.2$ for all the SEDs. The magenta long-dashed–short-dashed curve is the same as in the top panel of Fig. 3. We have included the energy values 1300 Å and 120 eV to guide the eye in the context of observations of Mrk 478 (see Section 3.3.2). Bottom panel: the stability curves corresponding to the ionizing continua shown in the top panels. With the growing strength of the *soft-excess* component, there is significant increase in the range of ξ_P over which thermally-stable warm gas at $\sim 10^5$ K can exist.

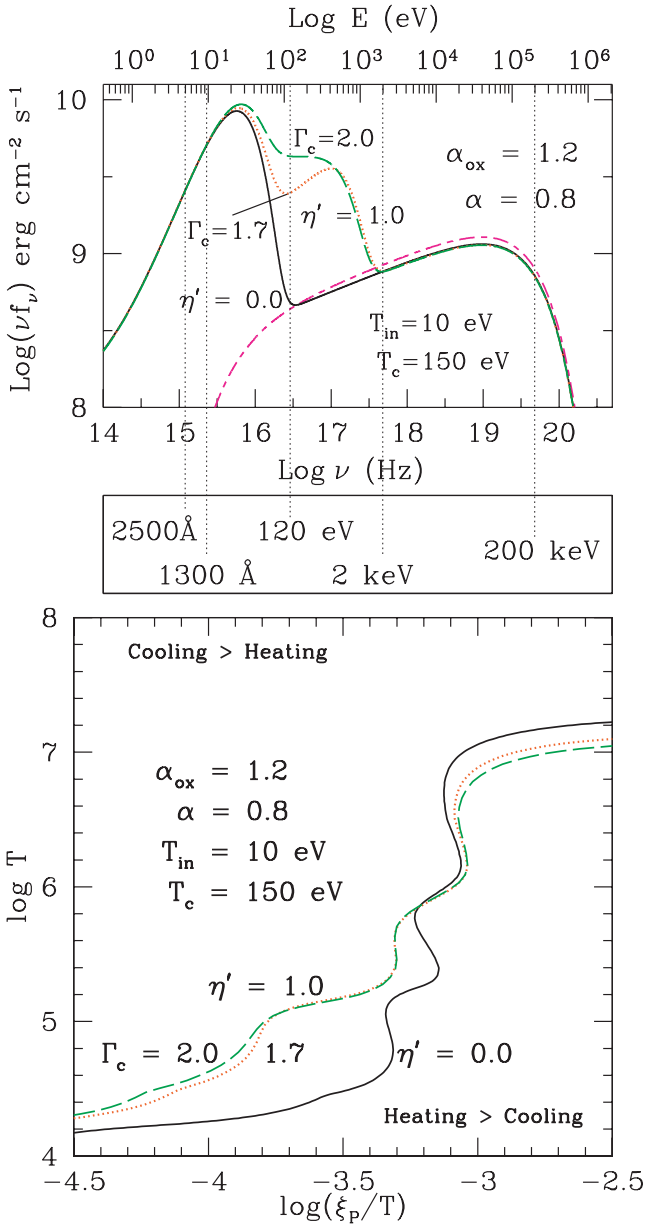

Figure 5. Top panel: ionizing continua with *soft-excess* component due to thermal Comptonization given by equation (5) with fixed values of $T_c = 150$ eV, $T_{in} = 10$ eV and $\eta' = 1.0$. The different curves are for different values of Γ_c, namely 1.7 and 2.0. For comparison, we have also drawn the continuum with no *soft excess* (solid curve). With $\alpha = 0.8$ and $\alpha_{OX} = 1.2$, the accretion disc component and the X-ray power-law component are the same for all the SEDs. The magenta long-dashed–short-dashed curve is the same as in the top panels of Figs 3 and 4. We have included the energy values 1300 Å and 120 eV to guide the eye in the context of observations of Mrk 478 (see Section 3.3.2). Bottom panel: the stability curves corresponding to the ionizing continua shown in the top panels.

panel, Fig. 4). We want to investigate if the alternative description of the *soft-excess* component, namely the *soft excess* due to thermal Comptonization, can account for a SED similar to that seen in Mrk 478, and observe its effects on the WA.

Spectra generated by equation (5) with fixed values of $T_c = 150$ eV, $T_{in} = 10$ eV and $\eta' = 1.0$ are drawn in the top panel of Fig. 5 for different values of Γ_c. For comparison, we have also drawn the continuum with no *soft excess* (Fig. 5, solid curves). The continuum with $\Gamma_c = 2.0$ satisfies the conditions required by observations of Mrk 478 as mentioned by Korista et al. (1997).

The influence of a thermal Comptonization *soft-excess* component on the stability curves is shown in the bottom panel of Fig. 5. We see again that the range of $\log(\xi_P/T)$ for the stable 10^5-K branch is increased in width from ~0.2 to 0.48 dex as η' goes from 0 to 1.0, independent of the value of Γ, facilitating the presence of a stable WA at these temperatures, and that the

different phases of the WA lose the possibility of existing in pressure equilibrium as the strength of the *soft-excess* component is increased.

The thermal Comptonized and the blackbody models of the *soft excess* result in similar WAs. For example, the $\eta = 1.0$ curves (dashed curve; lower panel of Fig. 4) has stable ranges of $\log(\xi_P/T)$ at 10^5 and 10^6 K similar to that of the $\eta' = 1.0$ curves (dotted and long-dashed curves for $\Gamma = 1.7$ and 2.0, respectively; lower panel of Fig. 5). The stability curves with $\eta' = 1.0$ do have a slightly smoother rise from $\sim 10^{4.2}$ to 10^5 K with no distinct intermediate unstable phase, because they have more flux in the $E = 10$–100 eV range for the same *soft-excess* strength.

4 CAUSE OF EXTENDED STABLE REGION: HEATING AGENTS AND ION FRACTIONS

We have observed that the disc-blackbody and the *soft-excess* radiation at $\lesssim 0.5$ keV significantly influence the stability curve, implying that these components are important for shaping the ionic and thermal state of the WA (Section 3). Changes in the *disc blackbody* affect the *low-temperature arm* ($\log T \sim 4.5$) of the stability curve, whereas the *soft excess* influences the absorbing gas at $\log T \sim 5.0$ K. In this section we examine the important heating agents and the distribution of ion fractions of the signature ions in the WA along the stability curve. All the ionizing continua considered in this section are given by equation (4). The effect of the thermal Comptonized *soft excess* gives the same qualitative results as the blackbody *soft excess* modelled by a blackbody (see equation 4).

4.1 Heating

CLOUDY works by dividing a gas into a set of thin concentric shells, referred to as 'zones' which have thicknesses that are small enough for the physical conditions across them to be nearly constant, maintained by continuously adjusting the physical thicknesses of these shells. For this subsection, only, we have constrained the code to perform a single-zone calculation for numerical convenience as we are not concerned with quantitative rigour, but want to understand the qualitative trends.

Fig. 6 shows the influence of these two components on the heating fraction ΔH of H^{+0}, He^{+1}, Fe and O as a function of ξ_P/T. All other ions and/or elements contribute less than 10 per cent to ΔH.

In the left-hand panels, the solid and dot–dashed curves, respectively, correspond to a WA ionized by an SED with $T_{in} = 10$ and 30 eV (see equation 4). In both cases $\eta = 0$ so that there is no *soft-excess* component in these SEDs, so any changes in the heating fractions are entirely due to the variation in the accretion disc spectrum.

In the right-hand panels, the solid and the dot–dashed curves correspond to $\eta = 0$ and 3, respectively, while $T_{in} = 10$ eV. Hence, changes in the heating fractions in the right-hand panels are due only to the varying strength of the *soft-excess* component.

The top panels (labelled A) of Fig. 6 show the region of the stability curves where the variation of these spectral components has maximum effect.

4.1.1 Hydrogen and helium

Panels B and C of Fig. 6 show the distribution of ΔH, respectively, for neutral hydrogen H^{+0} and singly ionized helium He^{+1}. In the left-hand panels, we see that there is no significant difference in the distributions as T_{in} increases from 10 to 30 eV. For both H^{+0} and He^{+1}, ΔH is considerably less for $\eta = 3.0$ than for $\eta = 0$ as seen in the right-hand panels. Thus in either case (of the disc blackbody or the *soft excess*) H^{+0} and He^{+1} can be ruled out as the cause of extra heating causing the increase in the temperature of the stability curves in the range of $\log(\xi_P/T)$.

4.1.2 Iron

We find that in the disc-blackbody and *soft-excess* cases the significant heating agents are the various species of iron. It is to be noted that the range of ΔH for Fe (panels D1, D2 and D3) is double that for O (panels E1, E2 and E3). The ΔH behaviour of the iron ions is affected both when we increase T_{in} from 10 to 30 eV, and when we increase η from 0 to 1. Fe^{+7}, Fe^{+8}, Fe^{+9}, Fe^{+10} and the Unresolved Transition Array (UTA, see below) are the most significant heating agents, and their contributions have been added to give the heating fraction due to iron (labelled 'Iron') in panels D1–D3. In the left-hand panels D2 and D3, the heating fractions of the individual ions of iron and the UTA are shown, respectively, for $T_{in} = 10$ and 30 eV. Similarly, the right-hand panels D2 and D3 show ΔH for the individual iron ions and the UTA, respectively, for $\eta = 0$ and 3.0. A WA which is overabundant in iron (Fields et al. 2005, 2007) and/or illuminated by a SED having photons facilitating absorption by iron will be warmer at relatively lower values of ξ_P. These two physical scenarios influence different ions of iron, which may help distinguish between the otherwise degenerate effects.

For $-4.0 < \log(\xi_P/T) < -3.4$, where ΔH for iron is most affected by T_{in}, Fe^{+8} and Fe^{+9} are the dominant ions (left-hand panels D2 and D3 of Fig. 6). The ionization potentials (IPs) for Fe^{+7}, Fe^{+8}, Fe^{+9} and Fe^{+10} are 151.1, 235, 262.1 and 290.4 eV, respectively. As the accretion disc becomes hotter, with T_{in} increasing from 10 to 30 eV, the number of photons with $E > 100$ eV increases by a factor of 27. It is this enhancement in the number of photons which influences these ions of iron differently in the two cases and hence changes the shape of the stability curves.

The UTA is a blend of the numerous absorption lines arising from the iron M-shell ions, Fe^{+0}–Fe^{+15}, due to their $n = 2$–3 (mainly 2p–3d, n being the principal quantum number of the active electron) transitions which are found to occur between 16 and 17 Å (730–776 eV) (Behar, Sako & Kahn 2001; Sako et al. 2001; Netzer 2004; Krongold et al. 2005a,b; Holczer et al. 2007). The energy ranges important for the UTA are likely to be influenced by the *soft-excess* component of the SED. This effect is clearly seen by comparing the ΔH distributions of the UTA in the right-hand panels D2 and D3 of Fig. 6; ΔH for iron is far more dominated by the UTA ΔH contribution for the $\eta = 3.0$ case in the range $-4.4 < \log(\xi_P/T) < 3.6$.

Note that in panels D2 (both the left-hand and right-hand side), the solid curve for iron is multivalued at $-3.43 < \log(\xi_P/T) < -3.42$, just where the stability curve is multivalued (see panels A), giving multiple phases in pressure equilibrium. On the other hand, for the $T_{in} = 30$ eV and $\eta = 3$ curves (the dot–dashed stability curves in panels A and the corresponding ΔH distribution of iron in panels D3, both the left-hand and right-hand side), there is no multivalued behaviour for $\log(\xi_P/T) \sim -3.4$. Thus, the behaviour of the stability curve seems to be driven by the heating due to the different ions of iron.

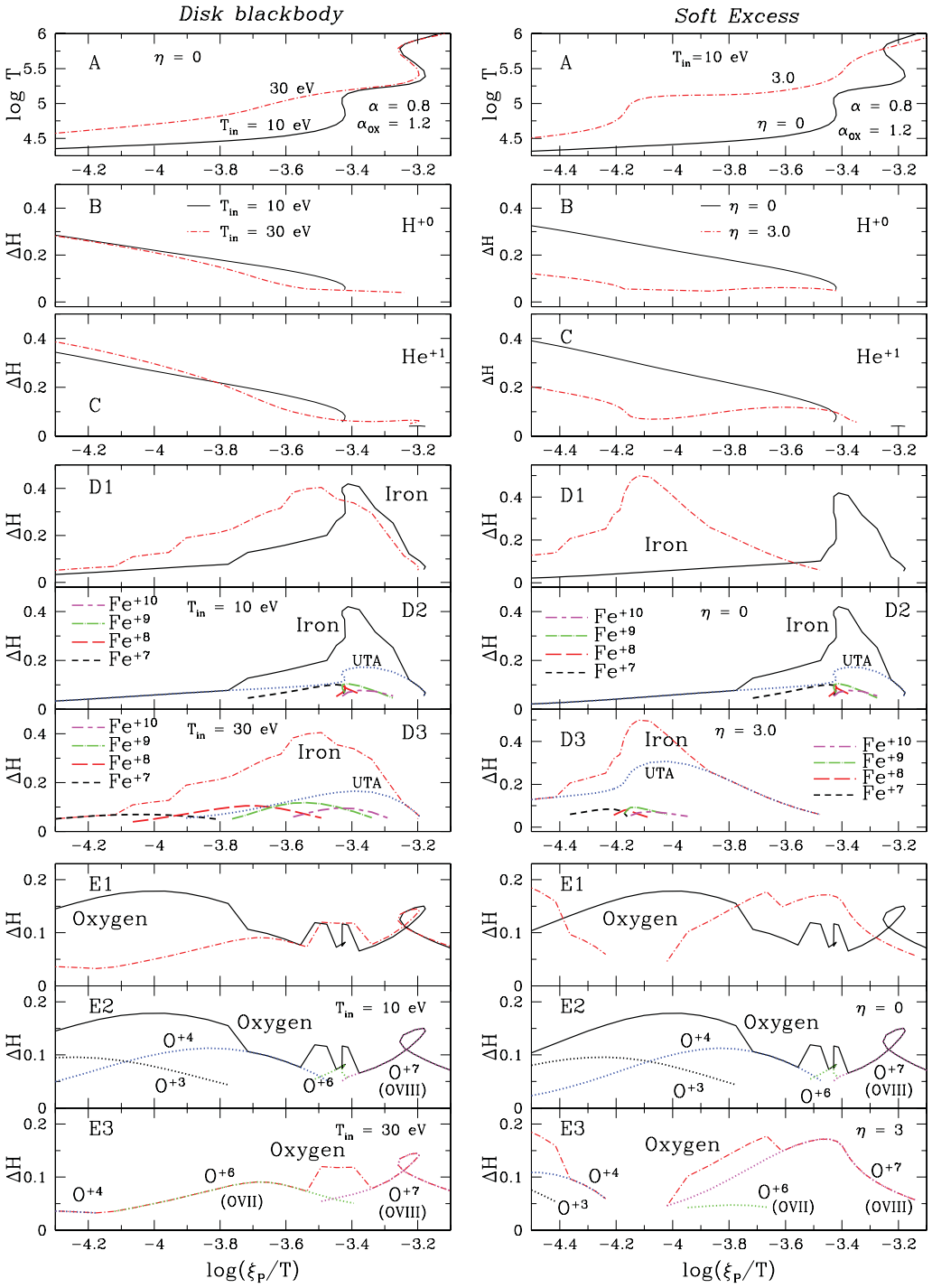

Figure 6. The principal heating agents that are being influenced by the soft spectral components *disc blackbody* (panels on the left-hand side) and *soft excess* (panels on the right-hand side) present in the SEDs of typical AGNs. Top panels (A): the stable part of the thermal equilibrium curves for an optically-thin solar metallicity gas illuminated by ionizing continua given by equation (4). In the left-hand panel, the solid and the dot–dashed lines correspond to SEDs having $T_{\rm in} = 10$ and 30 eV, respectively, with $\eta = 0$ in both cases. The solid line in the right-hand panel represents a SED with $\eta = 0$ and the dot–dashed curve is for $\eta = 1.0$, where $T_{\rm in} = 10$ eV for both the curves. We have zoomed-in on the regions of the stability curves where they differ most from each other. The line schemes described for the left-hand and right-hand panels are maintained the same as for the lower panels in the figure. Lower panels: fraction (ΔH) of the total heating caused by the various significant elements and ions. We have demonstrated the effects of all those elements which contribute $\gtrsim$10 per cent to the total heating in the same $\log(\xi_{\rm P}/T)$ range as shown in the top panels. Panels B, C, D1 and E1 show the results for H^{+0}, He^{+1}, iron and oxygen, respectively. The 'break-up' in heating fraction of iron is shown in panels D2 and D3 and the same for oxygen is shown in panels E2 and E3. Note that the y range for panels E1–E3 for oxygen is different from all other panels showing ΔH distributions because oxygen never contributes more than 20 per cent to the heating unlike other agents, some of which are responsible for even up to 50 per cent of the heating for some values of $\log(\xi_{\rm P}/T)$. Note that the discontinuity in the ΔH distribution of oxygen in the $\eta = 3.0$, $T_{\rm in} = 10$ eV case (dot–dashed curve in panels E1 and E3) is because the contribution drops below 5 per cent for $-4.2 < \log(\xi_{\rm P}/T) < 4.0$.

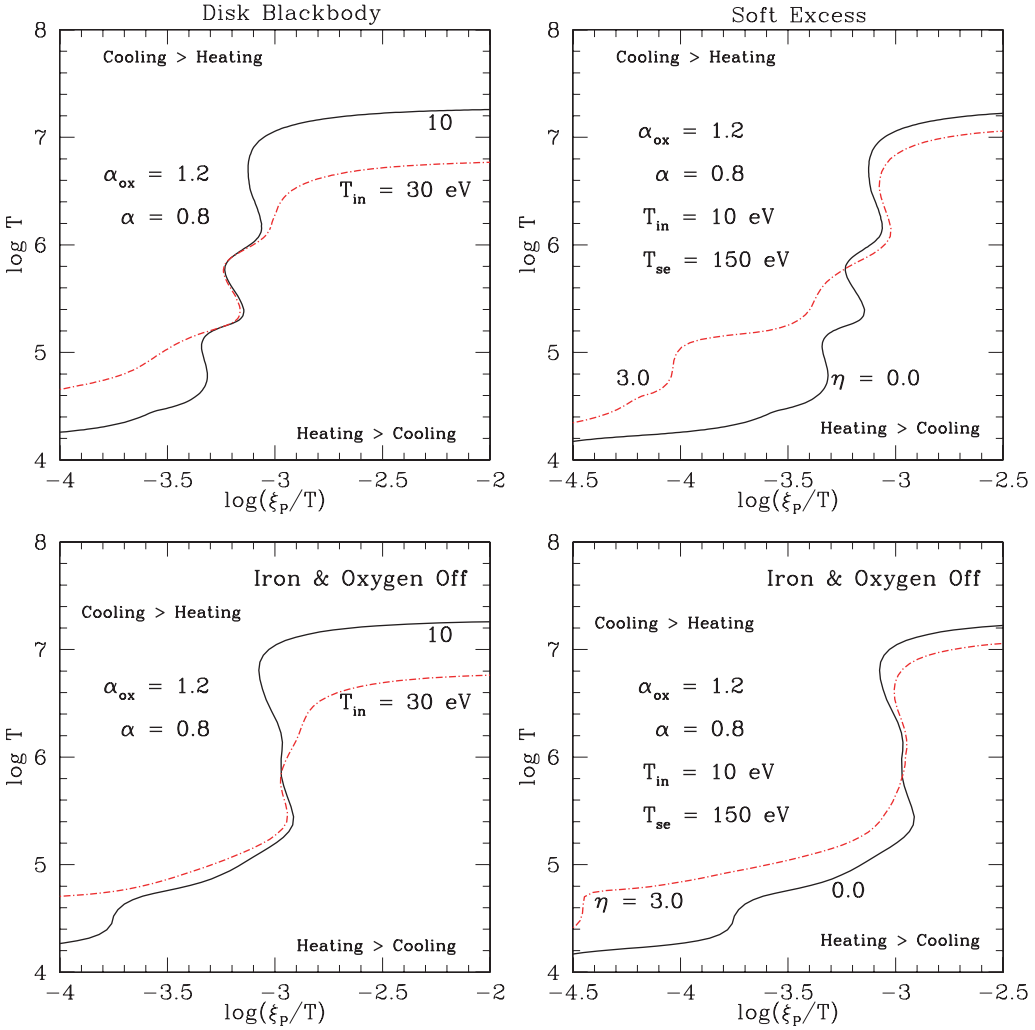

Figure 7. Top panels: the comparison between the stability curves for solar metallicity gas, when ionized by SEDs having accretion discs with different temperatures $T_{in} = 10$ and 30 eV (left-hand panels) and when the ionizing continua have different strengths of the *soft-excess* component $\eta = 0$ and 3.0 (right-hand panels). Bottom panels: the same ionizing continua are used to illuminate a gas for which iron and oxygen have been removed. The relative differences in the stability curves are almost entirely removed in the lower left-hand panel, and are significantly reduced in the lower right-hand panel, indicating that these spectral components strongly influence the ions of iron and oxygen.

4.1.3 Oxygen

Panels E1–E3 show the results for the heating fractions contributed by oxygen. Note the factor of 2 smaller, *y* range for the panels E1–E3 because oxygen never contributes more than 20 per cent to the heating of the gas.

The left-hand panels show that ΔH due to oxygen is lower for $T_{in} = 30$ eV than that for $T_{in} = 10$ eV in the range $\log(\xi/T) \lesssim -3.6$. In the same range of $\log(\xi/T)$, the stability curve for $T_{in} = 30$ eV has higher temperature than the $T_{in} = 10$ eV curve (panel A on the left-hand side). Thus, here oxygen is not acting as one of the required heating agents resulting in a warmer absorber.

However, in the $\eta = 3.0$ case (right-hand panels) oxygen becomes a significant excess heating agent for $\log(\xi_P/T) > -3.6$ where the contributing ions are O^{+6} (O VII) and O^{+7} (O VIII).

As for iron, the ΔH distribution due to oxygen for the $T_{in} = 10$ eV, $\eta = 0$ case, is also multivalued at the same values, namely the narrow range $-3.43 < \log(\xi_P/T) < 3.42$ (panels E2, both the left-hand and right-hand side), although not as strongly as that for iron (panels D2, both the left-hand and right-hand side). Moreover, at $\log(\xi_P/T) \sim -3.4$, it is iron and not oxygen which is the dominant heating agent. However, oxygen is the dominant heating agent at higher values, $\log(\xi_P/T) \sim -3.2$, and has multivalued ΔH distribution which drives the multiphase nature of the solid stability curves at those values of $\log(\xi_P/T)$.

The ΔH distribution of oxygen for the $T_{in} = 30$ eV, $\eta = 0$ case is shown in the left-hand panel E3 (dot–dashed curve). For $-3.8 < \log(\xi_P/T) \lesssim -3.3$, the oxygen ΔH is about two to four times lower than the iron ΔH (left-hand panel D3). The oxygen ΔH dominates only beyond $\log(\xi_P/T) > -3.3$ where it is multivalued and is responsible for the multivalued nature of the stability curve (left-hand panel A) at the same values of $\log(\xi_P/T)$.

For the $\eta = 3.0$, $T_{in} = 30$ eV case (right-hand panel E3) as well, the oxygen ΔH contribution is lower than the iron ΔH (right-hand panel D3) until $\log(\xi_P/T) \gtrsim -3.6$ beyond which the oxygen ΔH distribution determines the behaviour of the stability curve. Note that the stability curve (dot–dashed curve in the right-hand panel A) is not multivalued at $\log(\xi_P/T) \gtrsim -3.6$ because the ΔH for oxygen is not multivalued.

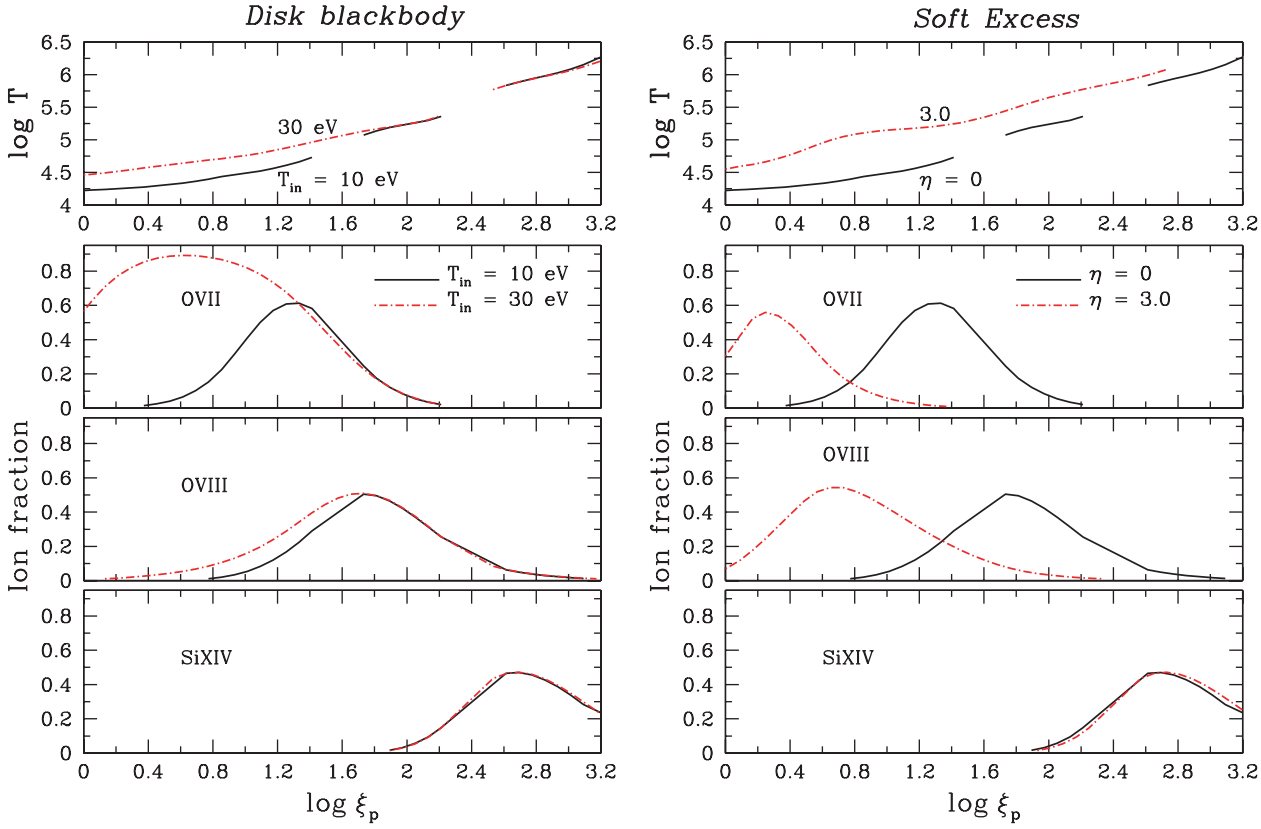

Figure 8. The ion fractions of some of the relevant ions as a function of ionization parameter; the left-hand panels show how this distribution is influenced by the *disc-blackbody* spectral component and the right-hand panels show the same for the *soft excess*. *Top panels*: the distribution of temperature as a function of ξ_P is plotted for the thermally-stable WA. The gaps in the curves correspond to the range of ξ_P over which the stability curve is thermally unstable. An increase in accretion disc temperature T_{in} from 10 to 30 eV makes the gas stable at $\log T \sim 5$. When the strength of the *soft excess* is increased from $\eta = 0$ to 3.0, all the phases of the WA become thermodynamically stable up to a temperature of $\log T \sim 6.3$. Lower panels: ion fraction for various ions (as labelled) important for the WA states. The line-style scheme followed here is the same as in Fig. 6 and is also labelled in the second panel from the top. See text for the physical implications of the ion fraction distribution.

Thus, at the higher ionization [$\log(\xi_P/T) \sim -3.2$] phase of the WA, the nature of the stability curve seems to be driven by the heating due to the oxygen ions, predominantly O^{+7} (O VIII).

4.1.4 Zero oxygen and iron abundance

We have further illustrated the importance of iron and oxygen as the key players in determining the thermal properties of the WA using Fig. 7. The distinction between the left-hand and right-hand panels is the same as that in Fig. 6; the upper panels have the same stability curves as in Fig. 6 (left-hand and right-hand panels A), but for slightly different ranges of $\log(\xi_P/T)$ and wider ranges of $\log T$.

Comparing the stability curves for solar metallicity gas (top panels), which have pronounced kinks in the temperature range $4.2 < \log T < 6.5$, with the relatively featureless ones for gas with zero O and Fe (bottom panels), we see that the detailed shape of the curves in the temperature range $\sim 4.2 < \log T < 6.5$ is governed by the atomic interactions due to oxygen and iron (also see Chakravorty et al. 2009). As a result, the SED-induced differences between the solid and dot–dashed stability curves in the top panels are significantly smoothed out in the bottom panels.

For $-3.7 < \log(\xi_P/T) < -3.3$ the rise in temperature of the solar metallicity stability curves in the top left-hand panel shows a temperature difference of 0.4 dex from one curve to the other. This difference is reduced to 0.2 dex when iron and oxygen are not present in the gas (lower left-hand panel), suggesting that a hotter accretion disc ($T_{in} = 30$ eV) mainly affects ions of iron and oxygen which results in a hotter WA.

The temperatures of the solar metallicity stability curves in the top right-hand panel are remarkably different, by $\sim$1 dex, for $-4.2 < \log(\xi_P/T) < -3.3$. These differences are significantly reduced to 0.3–0.5 dex when iron and oxygen are removed from the gas (lower right-hand panel). This indicates that atomic interactions due to these elements are affected by the strength of the *soft-excess* component. Unlike the accretion disc case, however, the stability curves in the lower right-hand panel retain some of their differences in WA temperatures, suggesting that other elements have a role as heating agents in the *soft-excess* case. The detailed investigation of this effect is beyond the scope of this paper, but will be attempted soon in our future publications.

4.2 Ion fraction

Absorption lines and edges of O VII, with IP of 0.74 keV, and O VIII, with IP of 0.87 keV, are often prominent signatures of the WA in soft X-ray spectra. Hence, the column densities of these two ions are often considered as important observable parameters for WA states (see the introduction for references). At higher values of ξ_P, absorption by various ions of silicon becomes important, for example, Netzer et al. (2003) show that Si XIV (IP of 2.67 keV) has a significant column density corresponding to the high-temperature component of the WA. We choose these three ions to study the

variation of their ion fraction as a function of ξ_P as the spectral components change in the ionizing continuum.

The ion fraction $I(X^{+i})$ of the X^{+i} ion is the fraction of the total number of atoms of the element X which are in the ith state of ionization. Thus,

$$I(X^{+i}) = \frac{N(X^{+i})}{f(X)N_H},$$

where $N(X^{+i})$ is the column density of the X^{+i} ion and $f(X) = n(X)/n_H$ is the ratio of the number density of the element X to that of hydrogen.

The top panels of Fig. 8 show the distribution of $\log T$ with respect to $\log \xi_P$ for the stable WA phases. The gaps in the lines correspond to the range of ionization parameters over which the gas is thermally unstable. The lower panels show I(O VII), I(O VIII) and I(Si XIV).

As before, the left-hand panels in Fig. 8 correspond to the changes in the disc blackbody. For $T_{in} = 10$ eV we can see three distinct regions of ξ_P separated by intermediate ranges of thermally unstable solutions. These regions are respectively dominated by O VII, O VIII and Si XIV. However, when T_{in} is raised to 30 eV, the stability curve becomes stable all the way up to $\log T = 5.3$ and the O VII-dominated phase gradually merges into the O VIII-dominated gas, as demonstrated by the uninterrupted dot–dashed line in the top left-hand panel. Thus, there seems to be a continuous distribution of possible thermal solutions resulting from the greater production of O VII (second panel from the top) which, in turn, is a result of the enhanced number of $E \gtrsim 100$ eV photons coming from a hotter accretion disc with $T_{in} = 30$ eV. The change in the shape of the *disc blackbody* does not change the ion fraction distribution of the high-ionization species like O VIII or Si XIV (the two lowest panels) or the stability curve for $\log T > 5$ and $\log \xi_P > 1.7$. Thus, the higher temperature ($\log T \gtrsim 5$) phase of the ionized absorber remains unaffected.

The effect of the *soft-excess* component is demonstrated in the right-hand panels of Fig. 8. In this case, the increase in the strength of the *soft-excess* component from $\eta = 0$ to 3.0 makes the absorber thermally stable all the way up to temperatures of $\log T \sim 6$. The third panel from the top shows that increase in the strength of the *soft-excess* component mainly influences the occurrence of O VIII. The fraction of O VII is reduced for $\eta = 3.0$ because of the facilitated production of O VIII at lower values of $\log \xi_P$. This is caused by increase in the number of ∼100 eV–2 keV photons by a factor of ∼7.5. The ion fraction distribution of Si XIV, however, remains unaffected (bottom panel).

5 OTHER SIGNIFICANT PHYSICAL PARAMETERS FROM EARLIER STUDIES

Chakravorty et al. (2009) had studied the properties of the WA as a function of the X-ray spectral index α and the chemical abundance of the gas. In this subsection, we summarize some of those results that are relevant in the context of the soft spectral components of typical AGN continua and their effect on the WA.

5.1 X-ray spectral index α

Chakravorty et al. (2009, section 5.1 and fig. 3) showed that there was no thermally-stable absorber for $\log T > 4.4$ for a flat spectral index of $\alpha = 0.2$ (in equation 2, $\alpha_{OX} = 1.2$). Fig. 9 shows the stability curve using equation (2) with $\alpha = 0.2$ (magenta dotted line), which corresponds to an ionizing continuum with no *soft-excess* component, and shows no appreciable stable WA phase at $T \sim 10^5$ K. In Section 3.3, we have seen that the presence of *soft-excess* component in the AGN spectra facilitates the existence of thermally-stable gas at $\log T \sim 5.0$. However, throughout we have used $\alpha = 0.8$. It is thus crucial to check if the *soft-excess* component can result in stable 10^5- K gas even if $\alpha \sim 0.2$.

The solid, dot–dashed and dashed curves in Fig. 9 show the comparison between the stability properties of the WA ionized by SEDs given by equation (4) with $T_{se} = 150$ eV, $\eta = 3.0$ and $T_{in} = 10$ eV but various values of α (0.8, 0.5 and 0.2). The range, in $\log(\xi/T)$, of stable WA phase at $\log T \sim 5$ decreases as a function of decreasing value of α. However, even for α as low as 0.2 we still see a stable phase at $\log T \sim 5$. Thus, the appearance of a stable state at $\log T \sim 5.0$ for the $\alpha = 0.2$ curve can be attributed to the presence of a strong *soft-excess* component present in the ionizing continuum. However, if $\alpha \lesssim 0.2$, even with contributions from a strong *soft-excess* component, there is no evidence for stable gas at any higher temperature than $\log T > 5.3$ (refer to the blue dashed curve).

Note that in Fig. 9 the stability curves are drawn using ξ instead of ξ_P. The normalization scheme for the ionization parameter discussed in Section 3.1 is not appropriate while comparing SEDs with different values of the X-ray spectral index α.

5.2 Chemical abundance of the absorber

We discuss the role of the elemental abundances of the absorbing medium in Chakravorty et al. (2009). Here, we revisit the super-solar metallicity results but with more realistic AGN continua given by equation (4) ($\alpha = 0.8$, $\eta = 3.0$ and $T_{in} = 10$ eV). The stability curves are shown in Fig. 10 for WA abundances from solar ($Z_\odot$)

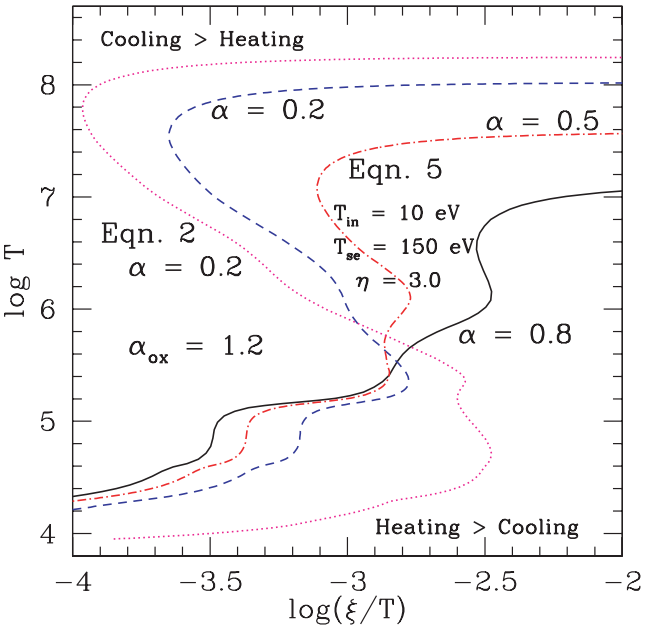

Figure 9. Thermal equilibrium curves generated using SEDs given by equation (4) with a strong *soft excess* ($T_{se} = 150$ eV, $\eta = 3.0$ and $T_{in} = 10$ eV) for a range of X-ray slopes $\alpha = 0.8$ 0.5 and 0.2 (respectively drawn with the solid, dot–dashed and dashed lines). In the stable phase at $\log T \sim 5.0$, the range of $\log(\xi/T)$ progressively decreases as α decreases from 0.8 to 0.5 and then to 0.2. For comparison we have used equation (2) with $\alpha = 0.2$, which corresponds to an ionizing continuum which has no *soft-excess* component, and drawn the dotted stability curve which is consistent with no stable WA phase at $\log T \sim 5.0$.

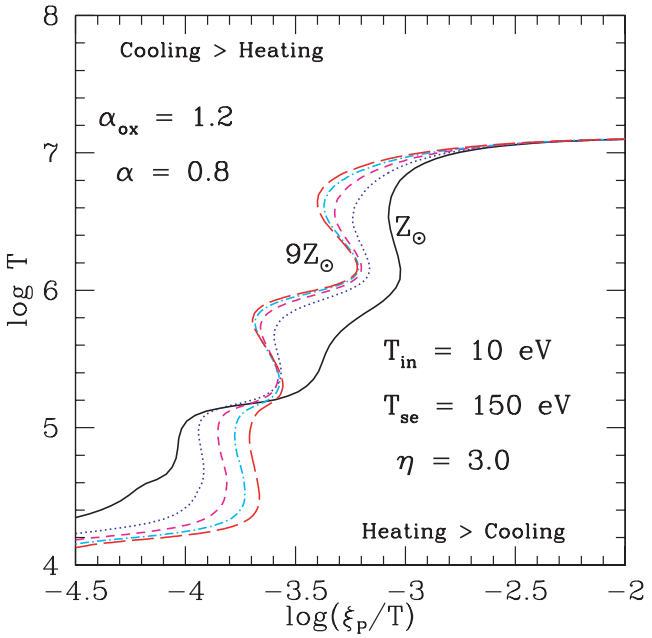

Figure 10. Stability curves for absorbers with solar and super-solar abundance from $Z_\odot$ to 9 $Z_\odot$ in steps of 2. The ionizing continuum has a strong soft excess (equation 4 with $\alpha = 0.8$, $\eta = 3.0$ and $T_{in} = 10$ eV).

to 9 $Z_\odot$ in steps of 2. The qualitative results are the same as in Chakravorty et al. (2009).

On the low-temperature ($\log T \lesssim 4.5$, corresponding to O VII-like ions) arm of the stability curves, super-solar metallicity results in a cooler absorber for the same ξ_P (or ξ) values, with an increase in the range of ξ_P over which we get a stable WA. Thus, super-solar metallicity opposes the role of increased T_{in} (see Fig. 3 in Section 3.2).

For the intermediate-temperature arm of the stability curve ($\log T \sim 5.0$, corresponding to O VIII-like ions) super-solar abundance decreases the range of stable WA, thus opposing the influence of the increase in η in the ionizing continuum (see Fig. 4 in Section 3.3).

On the highest temperature arm of the WA ($\log T \sim 6.0$, corresponding to Si XIV-like ions) super-solar gas tends to be hotter, and is thermodynamically stable for a larger range of values of $\log(\xi_P/T)$. Thus, the fine-tuning of ξ_P values to detect such species of ions is relaxed if the absorber has super-solar abundance, and the probability of detecting these high-ionization species is increased. In this regime, the influence of high metallicity is degenerate with the influence of increasing α in the ionizing continuum, but only if $\alpha \gtrsim 0.8$ (see Fig. 9 in Section 5.1).

6 MULTIPHASE WARM ABSORBER

The stability curves we have derived in the previous sections often contain segments that allow phases at different temperatures to occur at similar pressure ξ_P/T, indicating the possibility of two or more distinct WA phases within the same medium to exist at near pressure equilibrium. However, variations in some of the physical parameters can also result in the possibility of multiphase absorbers being lost.

Observationally, distinct phases in pressure equilibrium have been derived in a number of cases of WAs (Krongold et al. 2003; Netzer et al. 2003; Chelouche & Netzer 2005; Krongold et al. 2007; Andrade-Velazquez et al. 2010), while in other cases it has been claimed that there is a continuous range of ionization parameters (Ogle et al. 2004; Steenbrugge et al. 2005). Since a wide range of physical parameters have been studied in this paper and Chakravorty et al. (2009) for their effects on WA, we can now form a clearer picture of which physical conditions favour multiphase absorbers.

The *disc-blackbody* component from the accretion disc affects the lower temperature part of the stability curve (Sections 3 and 4). Fig. 3 shows that the stability curve (solid line) with $T_{in} = 10$ eV has a slim range $-3.34 \leq \log(\xi_P/T) \leq -3.31$ over which gas at low temperatures $\log T \lesssim 4.3$ can be in pressure equilibrium with the absorber at intermediate temperatures $\log T \lesssim 5.0$. However, as T_{in} is increased, all possibilities of such multiphase structure are lost; instead, the curve becomes stable in the intermediate temperature range, supporting a continuous distribution of allowed pressure and temperature in this phase space. Thus, cooler accretion discs support a multiphase WA, although for a narrow range of pressure.

An ionizing continuum having no *soft excess* (solid line in Figs 4 and 5) allows for a multiphase WA between $\log T \sim 5$ and 6. However, with the increase in the strength of the *soft-excess* component, the range of $\log(\xi_P/T)$, over which the possibility of multiphase WA exists, reduces from 0.09 dex for $\eta = 0$ to 0.006 dex for $\eta = 1.0$ and to 0 for $\eta = 3.0$.

Chakravorty et al. (2009) had emphasized that super-solar abundances increase the range of $\log(\xi/T)$ with the possibility of multiphase WA (also see Komossa & Mathur 2001). For example, as the metallicity of the gas was increased from 1.0 through 3.0 to 5.0, $\Delta_{45}[\log(\xi/T)]$ increased from 0.012 through 0.08 to 0.1, where $\Delta_{45}[\log(\xi/T)]$ gives the range of common values of $\log(\xi/T)$ over which the WA has stable phases at both $\sim 10^5$ and $\sim 10^4$ K. Beyond a metallicity of 5 $Z_\odot$, $\Delta_{45}[\log(\xi/T)]$ was found to drop because the range of $\log(\xi/T)$ for the $\sim 10^5$ K WA was found to decrease with increase in metallicity and became zero for a gas with metallicity 9 $Z_\odot$.

Similar trends are retained for the continua in this paper. As the metallicity of the gas is increased, keeping the ionizing continuum the same, the stable phases increasingly align along the same values of $\log(\xi_P/T)$ (Fig. 10), strongly suggesting the presence of multiphase WA. $\Delta_{45}[\log(\xi_P/T)]$ increases from 0 to 0.02 to 0.04 to 0.045 as metallicity is increased from solar to 3, 5 and 7 times solar. Beyond this high metallicity, $\Delta_{45}[\log(\xi_P/T)]$ becomes constant. There is an even more significant increase in $\Delta_{56}[\log(\xi_P/T)]$ from 0 to 0.03 to 0.08 to 0.11 to 0.13 with increase in metallicity from solar to 3, 5, 7 and 9 times solar.

For NGC 3783, Netzer et al. (2003) found three distinct phases of WA in near pressure equilibrium. In Fig. 10 we see that only for $Z = 9\,Z_\odot$ there is a very narrow range of 0.03 dex in which all three phases of the WA, at temperatures $\sim 10^4$, 10^5 and 10^6 K, are stable in the range $-3.69 \leq \log(\xi_P/T) \leq -3.66$. Interestingly, the stability curve for a much lower metallicity, $Z = 5\ Z_\odot$, gas but ionized by a continuum with weaker *soft excess* ($\eta = 1.0$, not shown in Fig. 10) shows the three phases in pressure equilibrium for a larger range of 0.08 dex for $-3.48 \leq \log(\xi_P/T) \leq -3.4$. Thus, it is easier (relatively lower super-solar metallicity) to have three phases in pressure equilibrium if the strength of the *soft excess* is lower. In all the physical conditions of the WA that were studied by Chakravorty et al. (2009), three phases of the WA were found to coexist in pressure equilibrium for still lower metallicity $\gtrsim 3\,Z_\odot$ which brings it down to observed values (e.g. see Fields et al. 2005, 2007, for Mrk 279). It is to be noted, however, that the continua used by Chakravorty et al. (2009) had no *soft-excess* component in them.

7 CONCLUSION

We have examined the effect of SEDs including hot discs and *soft-excess* spectral components in the energy 'blind spot' between 13 and 100 eV (equations 4 and 5) on WA. We investigated whether the spectral shapes can, in turn, be constrained from the observed properties of the WA.

We summarize our results as follows:

(i) The maximum temperature of the accretion disc component (see equation 4, Section 2.2) strongly affects on the low-temperature ($\log T \lesssim 4.5$) arm of the stability curve, the thermal properties of which are largely decided by the ions Fe^{+7} to Fe^{+10} and O^{+6} (O VII). This phase of WA becomes hotter and thermodynamically stable over a larger range of ξ when the ionizing continuum is hotter ($T_{\rm in} = 30$ eV) compared to $T_{\rm in} = 10$ eV. Thus, hotter accretion discs are more likely to produce WA phases characterized by ions having similar IPs to O VII. However, the possibility of this phase of WA being in pressure equilibrium with the higher temperature phases is eliminated in the hot disc cases as $\Delta_{45}[\log(\xi/T)]$ decreases from 0.03 for $T_{\rm in} = 10$ eV to 0 for $T_{\rm in} =$ 20 and 30 eV. Changes in the accretion disc temperature, however, do not affect the higher temperature arms of the stability curve.

(ii) The thermal properties of the intermediate-temperature ($\log T \sim 5.0$) branch of the stability curve are essentially determined by atomic interactions due to the different ions of iron and O VIII (IP = 0.87 keV). We find that with the increase in the relative strength η of the *soft-excess* component this 10^5-K stable phase of the WA spans a much larger range of $\log(\xi/T)$ (by 0.4 dex from $\eta = 0$ to 3.0), thus increasing the probability of finding WA phases characterized by 'O VIII-like' ions.

(iii) For a gas whose chemical composition is devoid of iron and oxygen, changes in the accretion disc spectral component bring about no change in the properties of the WA, and changes due to the variation in the strength of the *soft-excess* component are significantly reduced.

(iv) The highest temperature arm ($\log T \sim 6.0$) of the stability curve which is characterized by the ions having similar IP to that of Si XIV (IP = 2.67 keV) is left almost unaffected by any changes either in the accretion disc component or in the *soft-excess* component.

(v) An AGN continuum with a flat X-ray slope will not produce high-IP ions like Si XIV, and may show signatures of lower IP ions like O VIII (IP = 0.87 keV) only if a sufficiently strong *soft-excess* component is present in the SED.

(vi) The metallicity of the gas plays an important role in determining the multiphase nature of the WA. The possibility of the 10^4- and 10^5-K phases of WA occurring at similar values of $\log(\xi/T)$ is increased if the absorber is super-solar in abundance. Similarly, the chances of having pressure equilibrium between the 10^5- and 10^6-K phases are also increased by the super-solar metallicity of the gas. However, all three phases, together, are found to be in pressure equilibrium only if $Z > 3\,Z_\odot$, and the required abundance to achieve this is increased if the ionizing continuum has stronger *soft excess*.

ACKNOWLEDGMENT

SC sincerely thanks Prof. Andy Fabian and Prof. Hagai Netzer for providing valuable suggestions in the early stage of preparing this paper.

REFERENCES

Allende Prieto C., Lambert D. L., Asplund M., 2001, ApJ, 556, L63
Allende Prieto C., Lambert D. L., Asplund M., 2002, ApJ, 573, L137
Andrade Velazquez M., Krongold Y., Elvis M., Nicastro F., Brickhouse N., Binette L., Mathur S., Jimenez-Bailon E., 2010, ApJ, 711, 888
Arnaud K. A., 1996, in Jacoby G. H., Barnes J., eds, ASP Conf. Ser. Vol. 101, Astronomical Data Analysis Software and Systems V. Astron. Soc. Pac., San Francisco, p. 17
Bechtold J. et al., 1994, AJ, 108, 759
Behar E., 2009, ApJ, 703, 1346
Behar E., Sako M., Kahn S., 2001, ApJ, 563, 497
Beloborodov A. M., 1999, in Poutanen J., Svensson R., eds, ASP Conf. Ser. Vol. 161, High Energy Processes in Accreting Black Holes. Astron. Soc. Pac., San Francisco, p. 295
Blustin A. J. et al., 2003, A&A, 403, 481
Brinkmann W., 1992, A&A, 254, 460
Buehler P., Courvoisier T. J.-L., Staubert R., Brunner H., Lamer G., 1995, A&A, 295, 309
Chakravorty S., Kembhavi A. K., Elvis M., Ferland G., Badnell N. R., 2008, MNRAS, 384, L24
Chakravorty S., Kembhavi A. K., Elvis M., Ferland G., 2009, MNRAS, 393, 83
Chelouche D., Netzer H., 2005, ApJ, 625, 95
Collinge M. J. et al., 2001, ApJ, 557, 2
Coppi P. S., 1992, MNRAS, 258, 657
Coppi P. S., 1999, in Poutanen J., Svensson R., eds, ASP Conf. Ser. Vol. 161, High Energy Processes in Accreting Black Holes. Astron. Soc. Pac., San Francisco, p. 375
Crummy J., Fabian A. C., Gallo L., Ross R., 2006, MNRAS, 365, 1067
Czerny B., Elvis M., 1987, ApJ, 321, 305
Elvis M., Wilkes B. J., Tananbaum H., 1985, ApJ, 292, 357
Elvis M., Green R. F., Bechtold J., Schmidt M., Neugebauer G., Soifer B. T., Matthews K., Fabbiano G., 1986, ApJ, 310, 291
Elvis M. et al., 1994, ApJS, 95, 1
Ferland G. J., Korista K. T., Verner D. A., Ferguson J. W., Kingdon J. B., Verner E. M., 1998, PASP, 110, 761
Fields D. L., Mathur S., Pogge R., Nicastro F., Komossa S., Krongold Y., 2005, ApJ, 634, 928
Fields D. L., Mathur S., Krongold Y., Williams R., Nicastro F., 2007, ApJ, 666, 828
Frank J., King A., Raine D., 2002, Accretion Power in Astrophysics, 3rd edn. Cambridge Univ. Press, Cambridge
Gehrels N., Williams E. D., 1993, ApJ, 418, L25
George I. M., Turner T. J., Netzer H., Nandra K., Mushotzky R. F., Yaqoob T., 1998, ApJS, 114, 73
Gierlinski M., Done C., 2004, MNRAS, 349, L7
Gondhalekar P. M., Kellett B. J., Pounds K. A., Matthews L., Quenby J. J., 1994, MNRAS, 268, 973
Green P. J. et al., 2009, ApJ, 690, 644
Grevesse N., Sauval A. J., 1998, Space Sci. Rev., 85, 161
Grupe D., Mathur S., Wilkes B., Osmer P., 2006, AJ, 131, 55
Haardt F., Maraschi L., 1993, ApJ, 413, 507
Halpern J. P., 1984, ApJ, 281, 90
Hess C. J., Kahn S. M., Paerels F. B. S., 1997, ApJ, 478, 94
Holczer T., Behar E., Kaspi S., 2007, ApJ, 663, 799
Holweger H., 2001, in Wimmer-Schweingruber R. F., ed., AIP Conf. Proc. Vol. 598, Solar and Galactic Composition. Am. Inst. Phys., New York, p. 23
Kaastra J. S., Steenbrugge K. C., Raassen A. J. J., van der Meer R. L. J., Brinkman A. C., Liedahl D. A., Behar E., de Rosa A., 2002, A&A, 386, 427
Kinkhabwala A. et al., 2002, ApJ, 575, 732
Komossa S., Mathur S., 2001, A&A, 374, 914
Komossa S., Meerschweinchen J., 2000, A&A, 354, 411
Korista K., Ferland G., Baldwin J., 1997, ApJ, 487, 555
Krolik J., Kriss G. A., 2001, ApJ, 561, 684

Krolik J. H., McKee C. F., Tarter C. B., 1981, ApJ, 249, 422
Krongold Y., Nicastro F., Brickhouse N. S., Elvis M., Liedahl D. A., Mathur S., 2003, ApJ, 597, 832
Krongold Y., Nicastro F., Elvis M., Brickhouse N. S., Mathur S., Zezas A., 2005a, ApJ, 620, 165
Krongold Y., Nicastro F., Brickhouse N. S., Elvis M., Mathur S., 2005b, ApJ, 622, 842
Krongold Y., Nicastro F., Elvis M., Brickhouse N., Binette L., Mathur S., Jimènez-Bailón E., 2007, ApJ, 659, 1022
Laor A., 1990, MNRAS, 246, 369
Laor A., Fiore F., Elvis M., Wilkes B. J., McDowell J. C., 1997, ApJ, 477, 93
Lightman A. P., Zdziarski A. A., 1987, ApJ, 319, 643
Lopez L. A., Brandt W. N., Vignali C., Schneider D. P., Chartas G., Garmire G. P., 2006, AJ, 131, 1914
Lynden Bell D., 1969, Nat, 223, 690
Makishima K., Maejima Y., Mitsuda K., Bradt H. V., Remillard R. A., Tuohy I. R., Hoshi R., Nakagawa M., 1986, ApJ, 308, 635
Malkan M. A., Sargent W. L. W., 1982, ApJ, 254, 22
Marshall H. L., Carone T. E., Shull J. M., Malkan M. A., Elvis M., 1996, ApJ, 457, 169
Mathews W. G., Ferland G. J., 1987, ApJ, 323, 456
Matsumoto C., Leighly K. M., Marshall H. L., 2004, ApJ, 603, 456
Mitsuda K. et al., 1984, PASJ, 36, 741
Nandra K., Pounds K. A., 1994, MNRAS, 268, 405
Netzer H., 1985, MNRAS, 216, 63
Netzer H., 1987, MNRAS, 225, 55
Netzer H., 1993, ApJ, 411, 594
Netzer H., 2004, ApJ, 604, 551
Netzer H. et al., 2003, ApJ, 599, 933
Neugebauer G., Oke J. B., Becklin E. E., Matthews K., 1979, ApJ, 230, 79
Ogle P. M., Mason K. O., Page M. J., Salvi N. J., Cordova F. A., McHardy I. M., Priedhorsky W. C., 2004, ApJ, 606, 151
Page K. L., Reeves J. N., O'Brien P. T., Turner M. J. L., Worrall D. M., 2004a, MNRAS, 353, 133
Page K. L., Schartel N., Turner M. J. L., O'Brien P. T., 2004b, MNRAS, 352, 523
Piconcelli E., Jimenez-Bailon E., Guainazzi M., Schartel N., Rodriguez-Pascual P. M., Santos-Lleo M., 2005, A&A, 432, 835
Porquet D., Reeves J. N., O'Brien P., Brinkmann W., 2004, A&A, 422, 85
Pounds K., Reeves J., 2002, preprint (astro-ph/0201436)
Pringle J. E., Rees M. J., Pacholczyk A. G., 1973, A&A, 29, 179
Reynolds C. S., 1997, MNRAS, 286, 513
Reynolds C. S., Fabian A. C., 1995, MNRAS, 273, 1167
Ross R. R., Fabian A. C., 1993, MNRAS, 261, 74
Ross R. R., Fabian A. C., 2005, MNRAS, 358, 211
Rybicki G. B., Lightman A. P., 1986, Radiative Processes in Astrophysics. John Wiley & Sons, Inc., New York
Sako M. et al., 2001, A&A, 365, L168
Shakura N. I., Sunyaev R. A., 1973, A&A, 24, 337
Shang Z. et al., 2005, ApJ, 619, 41
Shields G. A., 1978, Nat, 272, 706
Siemiginowska A., Kuhn O., Elvis M., Fiore F., McDowell J., Wilkes B. J., 1995, ApJ, 454, 77
Sobolewska M. A., Siemiginowska A., Zycki P. T., 2004a, ApJ, 608, 80
Sobolewska M. A., Siemiginowska A., Zycki P. T., 2004b, ApJ, 617, 102
Stalin C. S., Petitjean P., Srianand R., Fox A. J., Coppolani F., Schwope A., 2010, MNRAS, 401, 294
Steenbrugge K. C. et al., 2005, A&A, 434, 569
Tananbaum H. et al., 1979, ApJ, 234, L9
Tarter C. B., Tucker W., Salpeter E. E., 1969, ApJ, 156, 943
Tueller J., Mushotzky R. F., Barthelmy S., Cannizzo J. K., Gehrels N., Markwardt C. B., Skinner G. K., Winter L. M., 2008, ApJ, 681, 113
Turner A. K., Fabian A. C., Lee J. C., Vaughan S., 2004, MNRAS, 353, 319
Vignali C., Brandt W. N., Boller T., Fabian A. C., Vaughan S., 2004, MNRAS, 347, 854
Wilkes B. J., Elvis M., 1987, ApJ, 323, 243
Zdziarski A. A., Johnson W. N., Magdziarz P., 1996, MNRAS, 283, 193
Zheng W., Kriss G. A., Telfer R. C., Grimes J. P., Davidsen A. F., 1997, ApJ, 475, 469
Zycki P. T., Done C., Smith D. A., 1999, MNRAS, 309, 561

This paper has been typeset from a TEX/LATEX file prepared by the author.